

Nonthermal X-Rays from Supernova Remnant G330.2+1.0 and the Characteristics of its Central Compact Object

Sangwook Park¹, Oleg Kargaltsev², George G. Pavlov¹, Koji Mori³, Patrick O. Slane⁴, John P. Hughes⁵, David N. Burrows¹, and Gordon P. Garmire¹

ABSTRACT

We present results from our X-ray data analysis of the supernova remnant (SNR) G330.2+1.0 and its central compact object (CCO), CXOU J160103.1–513353 (J1601 hereafter). Using our *XMM-Newton* and *Chandra* observations, we find that the X-ray spectrum of J1601 can be described by neutron star atmosphere models ($T^\infty \sim 2.5\text{--}5.5$ MK). Assuming the distance of $d \sim 5$ kpc for J1601 as estimated for SNR G330.2+1.0, a small emission region of $R \sim 0.4\text{--}2$ km is implied. X-ray pulsations previously suggested by *Chandra* are not confirmed by the *XMM-Newton* data, and are likely not real. However, our timing analysis of the *XMM-Newton* data is limited by poor photon statistics, and thus pulsations with a relatively low amplitude (i.e., an intrinsic pulsed-fraction $< 40\%$) cannot be ruled out. Our results indicate that J1601 is a CCO similar to that in the Cassiopeia A SNR. X-ray emission from SNR G330.2+1.0 is dominated by power law continuum ($\Gamma \sim 2.1\text{--}2.5$) which primarily originates from thin filaments along the boundary shell. This X-ray spectrum implies synchrotron radiation from shock-accelerated electrons with an exponential roll-off frequency $\nu_{\text{rolloff}} \sim 2\text{--}3 \times 10^{17}$ Hz. For the measured widths of the X-ray filaments ($D \sim 0.3$ pc) and the estimated shock velocity ($v_s \sim \text{a few} \times 10^3$ km s⁻¹), a downstream magnetic field $B \sim 10\text{--}50$ μG is derived. The estimated maximum electron energy $E_{\text{max}} \sim 27\text{--}38$ TeV suggests that G330.2+1.0 is a candidate TeV γ -ray source. We detect faint thermal X-ray emission in G330.2+1.0. We estimate a low preshock density $n_0 \sim 0.1$ cm⁻³, which suggests a dominant contribution from an inverse Compton mechanism (than the proton-proton collision) to the prospective γ -ray emission. Follow-up deep radio, X-ray, and γ -ray observations will be essential to reveal the details of the shock parameters and the nature of particle accelerations in this SNR.

¹Department of Astronomy and Astrophysics, Pennsylvania State University, 525 Davey Laboratory, University Park, PA 16802; park@astro.psu.edu

²Department of Astronomy, University of Florida, Gainesville, FL 32611-2055

³Department of Applied Physics, University of Miyazaki, 1-1 Gakuen Kibana-dai Nishi, Miyazaki, 889-2192, Japan

⁴Harvard-Smithsonian Center for Astrophysics, 60 Garden Street, Cambridge, MA 02138

⁵Department of Physics and Astronomy, Rutgers University, 136 Frelinghuysen Road, Piscataway, NJ 08854-8019

Subject headings: stars: neutron — X-ray: stars — ISM: individual (SNR G330.2+1.0)
 — supernova remnants

1. INTRODUCTION

Since nonthermal X-ray synchrotron emission was discovered in portions of SN 1006’s blast wave shock (Koyama et al. 1995), several young supernova remnants (SNRs) now show such strong particle acceleration sites in the shock front. The detection of nonthermal X-ray emission in SNRs thus provides an excellent opportunity to study the generation of high energy cosmic-rays. Based on the archival *ASCA* data, Torii et al. (2006) discovered that the overall X-ray emission from the Galactic shell-type radio SNR G330.2+1.0 shows a featureless spectrum primarily from a power law (PL) continuum ($\Gamma \sim 2.8$). G330.2+1.0 is thus one of the rare members of Galactic SNRs in which X-ray emission is dominated by nonthermal continuum from synchrotron radiation of shock-accelerated relativistic electrons: there are only three other Galactic SNRs showing such characteristics, G347.3–0.5 (a. k. a. RX J1713.7–3946, Slane et al. 1999), G266.2–1.2 (a. k. a. RX J0852.0–4622 or “Vela Jr.”, Slane et al. 2001), and G1.9+0.3 (Reynolds et al. 2008). Torii et al. (2006) noted the general anti-correlation between the X-ray and radio intensities in G330.2+1.0, which may suggest multiple populations and/or acceleration processes to produce spatially separated X-ray and radio emission. The *ASCA* study of G330.2+1.0 was, however, limited by the low photon statistics (~ 2000 counts for the entire SNR) and poor angular resolution ($\sim 3'$ FWHM).

We observed G330.2+1.0 with *Chandra* to perform a detailed imaging and spectral study of the SNR, which could not be performed with the low angular resolution detectors on board *ASCA* (Park et al. 2006). In our initial work on the *Chandra* data, we discovered a candidate neutron star (CXOU J160103.1–513353, J1601 hereafter) at the center of the SNR (Park et al. 2006). The featureless X-ray spectrum of J1601 is well-described by a black-body (BB) model with $T = 5.7$ MK. The high foreground column ($N_{\text{H}} \sim 2.5 \times 10^{22} \text{ cm}^{-2}$) is consistent with that for SNR G330.2+1.0, supporting their spatial association. Assuming the distance $d \sim 5$ kpc to G330.2+1.0 as estimated by the HI absorption (McClure-Griffiths et al. 2001), a small area ($R \sim 0.4$ km) for the BB region is implied. The observed X-ray luminosity is $L_{\text{X}} \sim 1 \times 10^{33} \text{ ergs s}^{-1}$ in the 1–10 keV band. No counterpart is found in the optical, IR, and radio bands, and a large X-ray-to-optical flux ratio ($f_{1-10 \text{ keV}}/f_{\text{V}} > 9$) is estimated. There is no evidence for long-term time variability (in the 1-7 keV band) up to ~ 10 hr time scales in the light curve of J1601. All these characteristics are typical for the peculiar manifestation of neutron stars found at the center of several SNRs, dubbed “Central Compact Objects (CCOs)” (Pavlov et al. 2002). A particularly intriguing aspect of J1601 is its possible pulsations (Park et al. 2006). Because of the low photon statistics (~ 600 counts) and the long frame-time (3.24 s) of the *Chandra* data, the detection of the periodicity ($P = 7.48$ s) was not conclusive ($\sim 2\sigma$ significance).

We have recently performed a follow-up observation of G330.2+1.0 and J1601 with *XMM-*

Newton to compensate the low photon statistics and poor time resolution of the *Chandra* data. When combined with the high angular resolution *Chandra* data, the good time resolution and large collecting area of *XMM-Newton* can help reveal the detailed nature of the SNR and the CCO. We report here the results from our analysis of G330.2+1.0 and J1601 using our *XMM-Newton* and *Chandra* data. Unfortunately, the *XMM-Newton* data are significantly contaminated by flaring background. Nonetheless, using the available data (*Chandra* + *XMM-Newton*), we derive some fundamental properties of J1601 and G330.2+1.0. In § 2, we describe the observations and the data reduction. X-ray spectral and timing analyses of J1601 are presented in § 3 and § 4, respectively. We present the spectral analysis of G330.2+1.0 in § 5. In § 6, we discuss implications on the results from data analysis of the CCO and SNR. Finally, a summary and conclusions are presented in § 7.

2. OBSERVATIONS & DATA REDUCTION

We observed G330.2+1.0/J1601 with the European Photon Imaging Camera (EPIC) on board *XMM-Newton* Observatory on 2008-03-20 (ObsID 0500300101). The pointing (RA[J2000] = $16^h 01^m 3^s 14$, Dec[J2000] = $-51^\circ 33' 53''.6$) is to J1601 which is positioned at the center of the nearly circular X-ray shell of SNR G330.2+1.0. We chose the small-window mode ($4'.4 \times 4'.3$ field of view [FOV] and 6 ms time resolution) for the EPIC pn to search for pulsations of J1601. We chose the full-window mode ($\sim 30'$ diameter FOV) for the EPIC MOS detectors to study the entire SNR. The medium filter was used for all detectors. We reduced the data using the Science Analysis System (SAS) software package v7.1.0.

Our *XMM-Newton* observations of G330.2+1.0/J1601 were significantly contaminated by flaring particle background. We removed time bins in which the overall count rate is 2σ (the pn) or 3σ (the MOS1 and MOS2) above the mean value for time intervals unaffected by flaring background. Time intervals including a considerable contamination by the flaring background ($\gtrsim 50\%$ above the average quiescent rate) were eliminated by these time-filters. After the time filtering, 26, 31, and 33 ks exposures for the pn¹, MOS1, and MOS2, respectively, are available for further data analysis, which is ~ 40 – 45% of the total exposure. We then reduced the data following the standard screening of event pattern (PATTERN ≤ 12 for the MOS1/2 and PATTERN ≤ 4 for the pn) and hot pixels (FLAG = 0). (For the timing analysis of J1601, we used a longer exposure while choosing a smaller aperture and more strict event pattern criteria as described in § 4.) There are stable components of instrumental background in the EPIC detectors. The primary components that could affect this work are Al-K ($E \sim 1.5$ keV) and Si-K ($E \sim 1.7$ keV) fluorescence lines due to the interactions of high energy particles with the structure surrounding the detectors and the detectors themselves². We removed these events from our image analysis by excluding narrow energy bands centered on these lines. Our background-subtracted source spectra show little evidence of these lines. Thus,

¹The $\sim 30\%$ deadtime-corrected exposure for the small window mode of the pn is 18.3 ks.

²*XMM-Newton* Users' Handbook, § 3.3.7.2.

we believe that the impact of contamination from this instrumental background on our EPIC data analysis is negligible.

Because of the severe contamination by the flaring background, photon statistics of the filtered *XMM-Newton* data are significantly lower than originally intended. Thus, in addition to the *XMM-Newton* data, we use the *Chandra* data (ObsID 6687) for the spectral analysis to improve overall photon statistics. The high angular resolution of *Chandra* data is also essential to measure the widths of the thin X-ray filaments of G330.2+1.0. We performed the *Chandra* observation of G330.2+1.0 with the I-array of the Advanced CCD Imaging Spectrometer (ACIS) on 2006-05-22 as part of the Guaranteed Time Observations program. The effective exposure after the data screening is ~ 50 ks, and thus photon statistics for the SNR and CCO in the ACIS data are similar to those obtained by the EPIC MOS1+MOS2 data. The details of the *Chandra* observation and data reduction are described by Park et al. (2006).

3. X-Ray Spectrum of the Central Compact Object

We extracted the spectrum of J1601 (~ 530 , 290, and 310 counts in the 0.5–10 keV band for the pn, MOS1, and MOS2, respectively) from a circular region with a radius of $15''$. The background spectrum was estimated from two nearby source-free regions with a radius of $30''$. The background counts contribute $\sim 15\%$ to the pn spectrum and $\sim 9\%$ to the MOS spectra. The background-subtracted, deadtime-corrected count rates (in the $15''$ radius aperture) are ~ 0.025 (pn) and ~ 0.009 counts s^{-1} (MOS1/2). The *Chandra* spectrum of J1601 was extracted from an $\sim 2''$ circular region. The background spectrum was extracted from the surrounding annular region with the inner and outer radii of $4''$ and $15''$, respectively (Park et al. 2006). The background-subtracted ACIS count rate is ~ 0.012 counts s^{-1} . The total source counts combining all the *XMM-Newton* EPIC and *Chandra* ACIS data are ~ 1700 counts, which is about three times higher than those used in the previous work. Each source spectrum was binned to contain a minimum of 20 counts per energy bin.

We simultaneously fit four spectra of J1601 obtained by the *XMM-Newton* pn, MOS1, MOS2, and the *Chandra* ACIS. Initially we fit the spectrum with a BB model. The best-fit BB temperature and the absorbing column ($T_{\text{BB}} = 5.6_{-0.4}^{+0.3}$ MK, $N_{\text{H}} = 2.46_{-0.35}^{+0.38} \times 10^{22}$ cm^{-2} , $\chi^2/\nu = 73.4/74$, errors are at 90% confidence level [C.L.], hereafter) are consistent with those by Park et al. (2006). The implied emitting area is small ($R \sim 0.44 d_5$ km, where d_5 is the distance to the CCO in units of 5 kpc), which is also in agreement with the previous work. The observed flux ($f_{\text{X}} \sim 1.22 \times 10^{-13}$ ergs cm^{-2} s^{-1} in the 1–10 keV band) is consistent with the previous *Chandra* results as well. Although a PL model may also fit the data, a very steep photon index ($\Gamma = 5.6_{-0.4}^{+0.5}$) and a high $N_{\text{H}} = 5.4 \pm 0.6 \times 10^{22}$ cm^{-2} ($\chi^2/\nu = 93.6/74$) are implied (The PL fit is not acceptable with $\chi^2_\nu > 2$, when N_{H} is fixed at $2.5\text{--}3.0 \times 10^{22}$ cm^{-2}). This PL shape is too soft for typical synchrotron emission from the neutron star’s magnetosphere, and the fit is statistically worse than that by the BB model. Thus, we conclude that X-ray emission of J1601 is consistent with a BB spectrum.

Using only *XMM-Newton* data, we estimate the *same* flux ($f_{1-10\text{keV}} \sim 1.25 \times 10^{-13}$ ergs cm^{-2} s^{-1}), which indicates that flux variations in the two years between the *Chandra* (2006-05-22) and *XMM-Newton* (2008-03-20) observations are negligible ($\lesssim 5\%$).

While the BB model can fit the overall X-ray spectrum of J1601, it may not be physically adequate to describe thermal emission from a neutron star. A neutron star is not a perfect BB, and likely has an atmosphere whose emission from the outermost H-layer may dominate the observed spectrum (e.g., Pavlov & Zavlin 2000). The observed spectrum of the thermal radiation from a neutron star’s surface is substantially affected by the properties of its atmosphere such as chemical composition, magnetic field, gravity, and the energy-dependent opacities (Pavlov et al. 1995 and references therein). A typical observational effect may be a higher temperature and a smaller emitting area than the “true” values when the spectrum is fitted by a simple BB model (e.g., Zavlin et al. 1998; Pavlov et al. 2000). Therefore, taking advantage of the improved photon statistics in the *XMM-Newton* + *Chandra* data, we fit the observed X-ray spectrum of J1601 with a hydrogen neutron star atmosphere model (NSA model in XSPEC, Pavlov et al. 1995; Zavlin et al. 1996).

First, we fit the spectrum of J1601 with a single NSA model. The magnetic fields of CCOs may be significantly lower or higher than the “canonical” magnetic field of a pulsar, $B = 10^{12}$ G (e.g., Pavlov & Zavlin 2000; Biglami et al. 2003). Based on the lack of a strong absorption feature in the observed spectrum of J1601, which would be interpreted as an electron cyclotron line in an NSA spectrum, we can only exclude fields in the range of $\sim (2 - 8) \times 10^{11}$ G. We thus fit our spectrum using all three magnetic field values for which the NSA models are available in XSPEC: $B = 0$ (applicable for low fields, $B \lesssim 10^{10}$ G), 10^{12} , and 10^{13} G. We fix the neutron star mass and radius at the canonical values $M_{\text{ns}} = 1.4M_{\odot}$ and $R_{\text{ns}} = 10$ km, which correspond to the gravitational redshift parameter $g_r = (1 - 2GM_{\text{ns}}/R_{\text{ns}}c^2)^{1/2} = 0.766$, and vary the effective temperature, distance, and N_{H} . The fits are statistically acceptable for all three magnetic field values. For $B = 0$ and 10^{13} G, the redshifted best-fit effective temperatures, $T_{\text{eff}}^{\infty} = 2.6$ and 3.6 MK, respectively, are lower than the T_{BB} , while $T_{\text{eff}}^{\infty} = 5.7$ MK for $B = 10^{12}$ G is about the same as the BB temperature³. The best-fit N_{H} values, 3.1 , 2.4 , and 2.7×10^{22} cm^{-2} , for $B = 0$, 10^{12} , and 10^{13} G, respectively, are consistent with that for SNR G330.2+1.0 ($N_{\text{H}} \sim 2.5\text{--}3 \times 10^{22}$ cm^{-2}). The best-fit distances, 24 , 169 , and 55 kpc, for $B = 0$, 10^{12} , and 10^{13} G, respectively, are unreasonably large for a Galactic object. To reconcile them with the distance to the SNR ($d \sim 5$ kpc; McClure-Griffiths et al. 2001), we have to assume that the sizes of the X-ray emitting areas are much smaller than $R_{\text{ns}} = 10$ km

³The higher T_{eff} and the correspondingly larger distance in the $B = 10^{12}$ G NSA fit are caused by the fact that the high-energy part of the observed spectrum coincides with the low-energy wing of the the gravitationally redshifted electron cyclotron feature, centered at ≈ 9 keV. Therefore, the high-energy tail of the X-ray spectrum is much softer than those in the models with very low or very high magnetic fields. Although we cannot exclude this field value based on the observational data available, we note that the models with slightly lower fields ($B \sim 2\text{--}8 \times 10^{11}$ G) would not fit the data, while the models with higher fields (e.g., $B \gtrsim 2 \times 10^{12}$ G) would yield essentially the same results as the $B = 10^{13}$ G model.

($R \sim 2, 0.3,$ and 0.9 km for $B = 0, 10^{12},$ and 10^{13} G, respectively). Thus, although the fits with the $B = 0$ and 10^{13} G NSA models yield lower temperature and larger sizes than the BB fit, the observed emission cannot be interpreted as emitted from the entire neutron star surface.

Based on these results, it is natural to assume that the X-ray emission in J1601 originates from small hot spots on the neutron star’s surface, such as suggested for other CCOs (e.g., the CCO in Cassiopeia A, Pavlov et al. 2000). In this scenario, the observed thermal X-ray emission consists of two characteristic components: the hot component from a small region(s) and the cool emission from the rest of the stellar surface (e.g., Pavlov et al. 2000). Therefore, we fit the observed spectrum of J1601 with two-component NSA models, assuming $B = 0, 10^{12},$ or 10^{13} G, the same for both components. For the soft component, we fix the distance to the CCO and the size of the emitting region at $d = 5$ kpc and $R = 10$ km, respectively, while varying the surface temperature. For the hard component, both the distance and surface temperature are varied. The foreground column N_{H} is tied common for both components, and then is fitted. The results are summarized in Table 1. The X-ray spectrum of J1601 and the best-fit two-component NSA model with a high magnetic field ($B = 10^{13}$ G) are presented in Fig. 1. We note that, although the additional soft component is statistically not required, implying only an upper limit on the observed flux (e.g., $f_{1-10\text{keV}} < 5 \times 10^{-14}$ ergs cm^{-2} s^{-1} at 90% C.L.), the two-component model likely represents a physically more realistic picture than the one-component model to account for the small hot region implied by the single NSA model. Therefore, we hereafter discuss the spectral nature of J1601 based on the two-component NSA model fits.

4. Search for Pulsations from the Central Compact Object

Park et al. (2006) searched for X-ray pulsations from J1601 in the 50 ks *Chandra* ACIS observation (3.24 s time resolution) and reported a marginally significant (at a $\approx 2\sigma$ level) periodic signal ($P = 7.48$ s, a pulsed fraction $f_{\text{rmp}} \sim 30\%$). One of the goals of our follow-up *XMM-Newton* observation was to test the significance of the previously reported period candidate, and to search for periodicity outside the frequency range accessible with *Chandra* data (The EPIC pn in the small-window mode provides much better 6 ms resolution). However, as discussed in § 2, the flaring background hampered our timing analysis of the EPIC pn data. For the timing analysis, we performed the data reduction following the methods described in § 2, except that (1) we used 44 ks of uninterrupted pn data after removing major flares, (2) we extracted photons from a smaller circular aperture ($8''.4$ in radius) than the standard pointlike source extraction area for the EPIC ($15''$ in radius), and (3) we applied a stricter screening by selecting events with PATTERN = 0. After these data reduction, we obtained a total of 761 photons (including $\approx 30\%$ background). The arrival times of these photons were recalculated to the solar system barycenter using the SAS `barycen` tool. As with the *Chandra* data, we used the Z_m^2 test (Buccheri et al. 1983) to search for periodicities in the $5 \times 10^{-5} - 80$ Hz frequency range. We calculated Z_1^2 at 3.5×10^7 equally spaced frequencies, which corresponds to oversampling by a factor of 10 compared to the expected

width $T_{\text{span}}^{-1} \approx 22 \mu\text{Hz}$ of the Z_1^2 peaks, and guarantees that we miss no peaks. The most significant peaks we find have $Z_1^2 = 31.82, 31.68$, and 30.56 at $f = 72.363177(5)\text{Hz}$, $12.011894(5)\text{Hz}$, and $3.006574(5)\text{Hz}$. However, even for the maximum value of $Z_1^2 = 31.82$, the corresponding significance is low: only 56.5%, for the number of independent trials $\mathcal{N} = f_{\text{max}}T_{\text{span}} \approx 3.5 \times 10^6$. Therefore, most likely these peaks are due to the noise.

We also calculated Z_m^2 for $m = 1, 2$ around the tentative pulsation frequency ($f = 0.1336185\text{--}0.1336999 \text{ Hz}$) suggested by the *Chandra* data (Park et al. 2006). We find a broad peak, $Z_1^2 = 10.06$ at $f = 0.133661(5)\text{Hz}$, overlapping with the *Chandra* peak. However, even a single trial significance (assuming that the periodicity found in the *Chandra* data is real and hence the pulsation frequency is known) for the peak in the pn data is only marginal (2.7σ with the corresponding $f_p = 24\%$), while for a blind search significance of this peak is negligible.

Finally, we searched for periodicity in the combined *Chandra* and *XMM-Newton* data. Allowing for a non-zero period derivative typical for anomalous X-ray pulsars (AXPs), we calculate Z_1^2 on two-dimensional grid: $f = 5 \times 10^{-5} - 0.15 \text{ Hz}$ and $\dot{P} = 0 - 3 \times 10^{-13} \text{ s s}^{-1}$. The maximum value of Z_1^2 is 29.9 at $f = 0.1336615 \text{ Hz}$ and $\dot{P} = 5 \times 10^{-14} \text{ s s}^{-1}$. Although the frequency corresponding to the maximum Z_1^2 is consistent with that of the peak found in the *Chandra* data alone, the significance of the peak found in the joint data is very low. Thus, we conclude that the tentative 7.48 s periodicity reported with *Chandra* is not confirmed by the *XMM-Newton* data.

5. Spectral Analysis of the Supernova Remnant

XMM-Newton images of SNR G330.2+1.0 are presented in Fig. 2. Since the small-window mode was used for the pn, the SNR is detected only on the MOS detectors. The *Chandra* image has revealed that G330.2+1.0 is a shell-type SNR with enhanced emission in the thin SW and NE parts of the shell (Park et al. 2006). Our *XMM-Newton* images confirm this general morphology. We further reveal spectral variations across the SNR: i.e., the E region of the shell is softer than other regions (Fig. 3). Also, there is a faint hard extended feature at $\sim 2'$ SW from the CCO (marked with an arrow in Figs. 2 and 3). These features were not clearly seen in the *Chandra* data because of their positions in the ACIS-I chip gaps.

We extracted the spectra from bright portions of the SNR shell in SW and NE (Fig. 4). The SW spectrum was extracted from the $\sim 1' \times 3'$ brightest filament in the SW shell, which contains ~ 1700 counts ($\sim 25\%$ of them are background) for the MOS1+MOS2 data. This SW shell contains ~ 1300 counts (including $\sim 13\%$ background) for the ACIS-I data. The NE spectrum was extracted from a circular region ($\sim 30''$ in radius) in the NE parts of the shell. This region contains ~ 570 counts ($\sim 30\%$ of them are background) and ~ 540 counts (including $\sim 30\%$ background) for the MOS1+MOS2 and the ACIS-I, respectively. We used the 0.5–10 keV band spectrum for the spectral analysis, and the source spectra were binned to contain a minimum of 20 counts per energy bin. Because of the non-uniform particle background across the MOS detectors, the background

spectrum for the *XMM-Newton* data was carefully selected for faint extended sources. We chose a few background regions close to the source regions while avoiding any detected (by *Chandra*) point sources. We find generally consistent results between the background subtracted *XMM-Newton* spectra and the *Chandra* data. Thus, we believe that our background estimates for the *XMM-Newton* data are acceptable.

The X-ray spectra of G330.2+1.0 extracted from the SW and NE regions are shown in Fig. 5. Our *Chandra* and *XMM-Newton* data show featureless continuum-dominated spectra for the bright SW and NE filaments. For each region, we performed a simultaneous PL model fit for all the three spectra obtained by the MOS1, MOS2, and ACIS-I (Fig. 5). The best-fit parameters are presented in Table 2. The high absorbing column for the SNR shell is consistent with that for the CCO J1601, supporting the SNR-CCO association. The PL photon indices are typical for synchrotron emission from highly accelerated relativistic electrons. Thus, we fit these SW and NE shell spectra with the SRCUT model, which describes X-ray synchrotron emission from the shock-accelerated electrons that are also responsible for the observed radio counterpart (Reynolds 1998; Reynolds & Keohane 1999). We assume the radio spectral index $\alpha = 0.3$ (where $S_\nu \propto \nu^{-\alpha}$) as measured from the entire SNR (Green 2001). The results of the SRCUT model fits are presented in Table 3.

The spectrally-hard, extended emission feature at $\sim 2'$ SW of the CCO is faint: we obtain ~ 490 counts from this feature (MOS1+MOS1) in which $\sim 60\%$ of the photons are the background. There is no evidence for line features, and the X-ray spectrum may be fitted by a PL of $\Gamma \sim 2$ with N_{H} fixed at $2.6 \times 10^{22} \text{ cm}^{-2}$. This overall spectral shape, the filamentary morphology and size (about a few d_5 pc), and the proximity to J1601 raise an intriguing possibility that this feature might be related to the CCO (e.g., the pulsar wind nebula). Alternatively, it could be a part of the SNR shell. However, reliable spectral modeling of this faint feature is difficult because of the poor photon statistics. Thus, we do not attempt any further analysis or discussion on this feature. Follow-up deep X-ray observations are required to reveal the origin of this potentially intriguing feature.

On the other hand, the E parts of the SNR shell are spectrally softer than other regions (Figs. 2 and 3). The E region spectrum is extracted from an $\sim 1'.3 \times 2'$ region in the E parts of the shell (Figs. 4 and 6). This region contains ~ 730 counts ($\sim 45\%$ of them are background) for the MOS1+MOS2 data. Since the central part of this region falls in the ACIS-I chip gap, we use only the *XMM-Newton* data for the spectral analysis. The best-fit PL photon index for region E is significantly steeper ($\Gamma \sim 4\text{--}5$, $\chi_\nu^2 \sim 1.3\text{--}1.4$, depending on the assumed N_{H}) than those for the SW and NE regions. In fact, the PL of $\Gamma = 2.3$ (as an average for SW and NE shell) cannot fit the observed spectrum of region E ($\chi_\nu^2 \sim 1.8\text{--}3.2$, depending on assumed N_{H}) because of a soft excess emission at $E \lesssim 2 \text{ keV}$. This suggests the presence of soft thermal emission in the E part of the shell. Thus, we fit the region E spectrum with a plane-shock (PSHOCK) model (Borkowski et al. 2001). Since the photon statistics are poor for this faint feature, we fixed the metal abundances at the solar values (Anders & Grevesse 1989). Initially we fit the observed spectrum with a single PSHOCK

model, assuming that X-ray emission in region E is entirely thermal in origin. Then, we used a two-component model (PSHOCK + PL) assuming that there is underlying nonthermal emission as seen in the SW and NE filaments. Results from these two model fits are statistically indistinguishable ($\chi^2_\nu \sim 1.2$ for either model fit). The main difference is that the best-fit electron temperature ($kT = 1.4^{+0.9}_{-0.6}$ keV) for the single PSHOCK model appears to be somewhat higher than that for the PSHOCK + PL model ($kT = 0.7^{+1.3}_{-0.3}$ keV). The best-fit volume emission measure (EM) for the two-component model is higher by a factor of ~ 2 than that for the single PSHOCK model. Since the uncertainties of these measurements are large because of poor photon statistics, it is difficult to discriminate these modeled parameters. Thus, we assume plausible ranges of the best-fit electron temperature and emission measure in the following discussion, based on these two models: i.e., $kT \sim 0.7\text{--}1.4$ keV and $EM \sim 0.6\text{--}1.4 \times 10^{56}$ cm $^{-3}$. The results from the PSHOCK + PL model fit for the E region are summarized in Table 2.

6. Discussion

6.1. Characteristics of the Central Compact Object

The previous *Chandra* data analysis of J1601 revealed characteristics of a thermal spectrum, a location at the center of SNR G330.2+1.0, a pointlike morphology without any extended nebulosity, the absence of counterparts at other wavelengths, and a large limit on the X-ray-to-optical flux ratio (Park et al. 2006). J1601 also shows no evidence for long-term variability, which is confirmed by our new *XMM-Newton* data showing a constant X-ray flux ($f_{1\text{--}10\text{keV}} \sim 1.2 \times 10^{-13}$ ergs cm $^{-2}$ s $^{-1}$) over the ~ 2 yr period. Thus, J1601 is most likely the CCO associated with SNR G330.2+1.0. Park et al. (2006) noted that the BB temperature is higher than the surface temperature expected from the standard cooling of a young neutron star, and that the estimated emitting area is too small to be a neutron star. It was also noted by Park et al. (2006) that the suggested candidate pulsations with a long period, if confirmed, would have been typical for an AXP.

Our results from the *XMM-Newton* and *Chandra* data analysis indicate that the hot component emission ($T_h^\infty \sim 2.5\text{--}5.5$ MK, depending on the assumed B) must originate from a small region of $R_h \sim 0.4\text{--}2 d_5$ km. The estimated size of the hot region varies depending on the assumed values of the magnetic field and the distance to the CCO. Nonetheless, within the ranges of parameters that we consider in this work ($B = 0, 10^{12},$ or 10^{13} G, and $d = 5\text{--}10$ kpc), the size of the hot region is significantly smaller than the canonical size of the neutron star; i.e., the largest area could be $R_h \sim 4$ km, where $B = 0$ and $d = 10$ kpc. A small hot region(s) has been suggested in other CCOs, probably indicating X-ray emission from a locally-heated region such as the hot polar cap (e.g., Pavlov et al. 2000). On the other hand, the estimated surface temperature of the neutron star is significantly lower ($T_s^\infty < 1.5$ MK) than that of the hot region. According to the standard cooling curves of a neutron star (e.g., Tsuruta 1998; Yakovlev & Pethick 2004), this temperature limit corresponds to a lower limit of several $10^2\text{--}10^4$ yr for the neutron star’s age. This neutron

star age is in plausible agreement with the estimated age of SNR G330.2+1.0 (see §§ 6.2 and 6.3, and Torii et al. 2006). The overall characteristics such as the low T_s^∞ , the high T_h^∞ , and the small R_h are consistent with those found in the prototype CCOs in Galactic SNRs such as Cas A and Vela Jr. (Pavlov et al. 2000; Pavlov et al. 2001).

Since the X-ray flux from the small hot region contributes a significant fraction of the observed flux ($> 50\%$ of the total flux in the 1–10 keV band), the observed X-ray emission from J1601 may be expected to pulsate. However, our *XMM-Newton* data do not show any conclusive evidence for pulsations, indicating that the previously suggested pulsations are unlikely real. We note that the low photon statistics in the EPIC-pn data are not sufficient to detect pulsations with an intrinsic pulsed-fraction $f_p \lesssim 40\%$. With the combined *Chandra* and *XMM-Newton* data, the detection of pulsations with $f_p \lesssim 25\%$ is not feasible. Thus, the presence of an X-ray pulsar for J1601 is not ruled out by the current data. The neutron star’s magnetic field, which would provide critical information on the nature of the object, remains unknown. Deep X-ray observations of J1601 are required to make conclusive remarks on the nature of J1601 such as pulsations, magnetic field, age, and the origin of its X-ray emission.

6.2. Nonthermal X-Ray Emission of the Supernova Remnant

Our joint spectral analysis of the *XMM-Newton* and *Chandra* data of G330.2+1.0 shows that X-ray emission from the bright filaments of the SNR shell is dominated by a PL continuum. We find that this PL spectrum prevails for the most parts of the SNR, which was also suggested by a previous study (Torii et al. 2006). The best-fit PL model for the bright SW and NE regions of the shell indicates photon indices of $\Gamma \sim 2.1$ – 2.5 which are typical for synchrotron emission from shock-accelerated relativistic electrons. Although thermal plasma models may also fit the observed spectra, the estimated electron temperatures are high ($kT \sim 4$ – 5 keV), and low metal abundances ($\lesssim 0.1$ solar, Anders & Grevesse 1989) are required. While a thermal origin of X-ray emission from the SNR shell may not be completely ruled out by the current data, the estimated plasma temperature and abundances appear to be unusual for SNRs. Thus, except for region E (§ 6.3), we discuss this SNR based on the nonthermal interpretations of X-ray emission.

According to our SRCUT model fits of the SW and NE filaments, the best-fit exponential roll-off frequency, $\nu_{\text{rolloff}} \sim 1.6$ – 3.3×10^{17} Hz, is relatively high among Galactic SNRs (Reynolds & Keohane 1999), while being similar to those for SN 1006 (Bamba et al. 2003) and the bright TeV γ -ray emitting SNR G347.3–0.5 (Lazendic et al. 2004). If the particle (electron) acceleration is limited by synchrotron losses, the cutoff frequency corresponding to the maximum electron energy E_{max} is $\nu_m(\text{loss}) \propto B E_{\text{max}}^2(\text{loss})$. Since $E_{\text{max}}(\text{loss}) \propto B^{-\frac{1}{2}}$, $\nu_m(\text{loss})$ is independent of B , and depends only on the shock velocity: e.g., assuming a strong shock of the compression ratio of > 4 and the shock normal perpendicular to B , the cutoff frequency is $\nu_m(\text{loss}) \gtrsim 3 \times 10^{16} \eta v_3^2$ Hz, where v_3 is the shock velocity in units of 10^3 km s $^{-1}$, and the ratio of the electron scattering mean free path to the gyroradius $\eta \geq 1$ (e.g., Reynolds 1998; Lazendic et al. 2004). As discussed below and in § 6.3,

the shock velocity appears to be roughly $v_s \sim 4000 \text{ km s}^{-1}$ for G330.2+1.0, and thus we estimate $\nu_m(\text{loss}) \gtrsim 5 \times 10^{17} \text{ Hz}$. Unless the shock velocity is much higher and/or the particle acceleration is inefficient ($\eta \gg 1$), the estimated $\nu_m(\text{loss})$ is comparable with the observed ν_{rolloff} , suggesting that the particle acceleration of electrons in G330.2+1.0 is likely limited by synchrotron losses rather than the age of the SNR. The peak frequency of a synchrotron emitting electron is $\nu_p = 1.8 \times 10^{18} E_e^2 B \text{ Hz}$, where B is the postshock magnetic field perpendicular to the shock normal, and E_e is the electron energy. For $\nu_p \sim 7 \times 10^{17} \text{ Hz}$ (or $\sim 3 \text{ keV}$) representing the typical X-ray photons based on the observed spectrum of the nonthermal filaments in G330.2+1.0, the corresponding electron energy is $E_e = 0.62 B^{-\frac{1}{2}} \text{ ergs}$. The characteristic synchrotron loss time scale for such electrons can then be estimated to be $\tau_{\text{loss}} = 630 E_e^{-1} B^{-2} \text{ s} = 1017 B^{-\frac{3}{2}} \text{ s}$.

We estimate τ_{loss} by measuring the widths of the bright nonthermal filaments of G330.2+1.0 using *Chandra* images (Fig. 7). We construct projected intensity profiles across the bright SW filaments by averaging the photon counts (in $4''$ pixel bins) over the $40''$ segments along the filaments. We fit these 1-D intensity profiles with a Gaussian to estimate the widths of the filaments. We note that high resolution *Chandra* images of bright X-ray synchrotron filaments in young SNRs show typical substructures of a broad exponential downstream region and a much steeper flux decay in the upstream (e.g., Bamba et al. 2003). G330.2+1.0 is more distant than other young SNRs (that show bright nonthermal filaments), and the X-ray shell is relatively faint, which does not allow us to resolve such a substructure. Since the downstream region is observed to dominate the width of the filaments, we assume a negligible contribution from the upstream emission in the widths of the filaments to measure the *downstream* widths of the filaments with a simple Gaussian model. The measured widths are $\sim 12''\text{--}16''$ (FWHM) which correspond to physical sizes $D \sim 0.3\text{--}0.4 d_5 \text{ pc}$. Because of the far distance and faint surface brightness of G330.2+1.0, our width measurements could be an overestimate from superpositions of thinner filaments. Nonetheless, the estimated widths are comparable with an average value for the individual filaments in SN 1006 ($\sim 0.2 \text{ pc}$, Bamba et al. 2003). Therefore, we take our measurements as a first-order estimate, and certainly as an upper limit.

The advection distance of the downstream electrons from the shock is $D_{\text{ad}} = v_s \tau_{\text{loss}} r^{-1}$, where r is the compression ratio in the shock. Since the direct measurements of the shock velocity of G330.2+1.0 are not available, we consider some plausible estimates for the shock velocity based on several independent approaches. Assuming an electron-ion temperature equipartition in the postshock region, the detected thermal emission of G330.2+1.0 (region E) implies $v_s \sim 1000 \text{ km s}^{-1}$ (§ 6.3). This value may be considered as a lower limit for v_s , because the assumed temperature equilibration between electrons and ions may have not been established in relatively young SNRs with $v_s \gtrsim$ several 10^2 km s^{-1} (Ghavamian et al. 2007). G330.2+1.0 shows similar characteristics (e.g., the SNR age, ν_{rolloff} , and the physical width of the nonthermal filaments etc.) to those of G347.3–0.5 and SN 1006 in which the shock velocities are high ($v_s \sim 3000\text{--}4000 \text{ km s}^{-1}$, e.g., Parizot et al. 2006 and references therein). The ambient density for G330.2+1.0 ($n_0 \sim 0.1 \text{ cm}^{-3}$, § 6.3) is not unusually high compared with other SNRs (e.g., Bamba et al. 2003). Thus, the

actual shock velocity of G330.2+1.0 is likely higher than $v_s \sim 1000 \text{ km s}^{-1}$, perhaps close to $v_s \sim 3000\text{--}4000 \text{ km s}^{-1}$. In fact, models predict high shock velocities of $v_s \gtrsim 2000 \text{ km s}^{-1}$ for an efficient particle acceleration (e.g., Ellison et al. 2000;2004). Although a small sample is used, an empirical relationship between ν_{rolloff} and the physical width of the nonthermal filaments D is derived to be $\nu_{\text{rolloff}} D^{-2} = 2.6 \times 10^{27} \tau_{\text{SNR}}^{-2.96}$ for several young historical SNRs (Bamba et al. 2005). This empirical relation suggests an SNR age $\tau_{\text{SNR}} \sim 1000\text{--}1200 \text{ yr}$ for G330.2+1.0 for the measured $\nu_{\text{rolloff}} \sim 2\text{--}3 \times 10^{17} \text{ Hz}$. The inferred young age and the low ambient density suggest that the SNR may be in a free-expansion or an adiabatic phase, or could be in transition between the two. Assuming an adiabatic phase, the suggested SNR ages imply $v_s \sim 2300\text{--}2800 \text{ km s}^{-1}$ for the SNR radius of $R = 7.3 \text{ pc}$ (see § 6.3 for the SNR radius). For a free-expansion phase, $v_s \sim 5800\text{--}7000 \text{ km s}^{-1}$ is implied. These high velocities are consistent with those estimated for young SNRs showing an efficient particle acceleration (e.g. Parizot et al. 2006 and references therein). Thus, as a rough estimate by *averaging* several values discussed above, we for simplicity adopt a shock velocity $v_s \sim 4000 \text{ km s}^{-1}$ for G330.2+1.0. This shock velocity is admittedly not a measurement and thus only a crude first-order estimate. (We would allow a factor of ~ 2 uncertainty in this velocity estimate, and within this range, our conclusions as discussed below are not affected.)

Assuming $r \sim 5\text{--}8$ for an efficient particle acceleration (e.g., Ellison et al. 2007), we estimate $\tau_{\text{loss}} \sim 350\text{--}600 \text{ yr}$ for the measured $D \sim D_{\text{ad}} \sim 0.3 d_5 \text{ pc}$, and thus $B \sim 14\text{--}20 \mu\text{G}$. The maximum electron energy can be estimated by $E_{\text{max}} = 2.5 \times 10^{-7} \nu_{\text{rolloff}}^{\frac{1}{2}} B^{-\frac{1}{2}} \text{ TeV} = 100\text{--}144 B_{\mu\text{G}}^{-\frac{1}{2}} \text{ TeV}$, where $B_{\mu\text{G}}$ is the postshock magnetic field in units of μG (Reynolds & Keohane 1999; Lazendic et al. 2004). Thus, $E_{\text{max}} \sim 22\text{--}38 \text{ TeV}$ (depending on measured ν_{rolloff}) is derived. In addition, if we consider a geometrical projection effect in measuring the widths of the nonthermal filaments (e.g., the observed width is $\sim 4.6 \times$ the actual width assuming a spherical shock with an exponential emission profile, Ballet 2006), the estimated B can be a few times higher ($\sim 50 \mu\text{G}$).

The estimated E_{max} for G330.2+1.0 suggests that this SNR is a candidate γ -ray source. For instance, the γ -ray emission by the inverse Compton (IC) scattering off interstellar photons can be estimated by $E_\gamma \sim 5.1 \times 10^{-12} E_\star E_e^2 \text{ eV}$, where E_γ is the average final energy of the up-scattered photons, and E_\star is the typical energy for the seed photons (Tatischeff 2008). Using $E_\star \sim 7 \times 10^{-4} \text{ eV}$ for the cosmic microwave background (CMB) and $E_e = E_{\text{max}} \sim 30 \text{ TeV}$, we estimate $E_\gamma \sim 3 \text{ TeV}$. However, G330.2+1.0 is not identified in the H.E.S.S. Galactic plane survey catalog (Aharonian et al. 2006a). It is probably because G330.2+1.0 is more distant and thus apparently fainter than other TeV-bright SNRs (e.g., G347.3–0.5 and G266.2–1.2). The IC to synchrotron flux ratio $f_{\text{IC}}/f_{\text{syn}} = 8\pi U_{\text{rad}}/B^2 \sim 10 B_{\mu\text{G}}^{-2} \sim 0.004\text{--}0.1$ (where the energy density of the seed CMB photons $U_{\text{rad}} \sim 0.25 \text{ eV cm}^{-3}$) for the plausible range of $B \sim 10\text{--}50 \mu\text{G}$ in G330.2+1.0. These $f_{\text{IC}}/f_{\text{syn}}$ are in fact similar to the observed $f_{\text{TeV}}/f_{\text{X}}$ for SNRs G347.3–0.5 and G266.2–1.2 (e.g., Matsumoto et al. 2007 and references therein). Then, the overall X-ray flux of $f_{\text{syn}} \sim 10^{-11} \text{ ergs cm}^{-2} \text{ s}^{-1}$ for G330.2+1.0 (Torii et al. 2006) implies $f_{\text{IC}} \sim 10^{-13}\text{--}10^{-12} \text{ ergs cm}^{-2} \text{ s}^{-1}$. The sky position of G330.2+1.0 was at the edge of the H.E.S.S. survey, in which the exposure was short ($< 5 \text{ hr}$). Considering the small angular size ($\sim 10'$) of G330.2+1.0, which is close to the point spread

function of the H.E.S.S. (several arcminutes), and the short exposure in the survey, the estimated IC flux is likely close to or below the H.E.S.S. detection limit of $f \sim 10^{-12}$ ergs cm $^{-2}$ s $^{-1}$ at $E \gtrsim 1$ TeV (e.g., Aharonian et al. 2005). Thus, if the γ -ray emission from G330.2+1.0 is dominated by the IC process of the same electrons to produce X-ray synchrotron emission, the non-detection of G330.2+1.0 with the current H.E.S.S. survey data is not surprising. A deep search of γ -ray emission for G330.2+1.0 using ground-based TeV telescopes and *Fermi* (formerly *GLAST*) is warranted.

It is notable that nonthermal X-ray emission in G330.2+1.0 is generally anti-correlated with the radio emission (Torii et al. 2006). Our high resolution *Chandra* and *XMM-Newton* images reveal that there actually exist radio counterparts for the bright X-ray filaments in SW and NE, but the radio emission is faint (Fig. 3). The brightest radio emission is in the E parts of the SNR, where X-ray emission is faint and spectrally soft (Fig. 3). Thus, the bright radio emission likely traces high density regions where soft (thermal) X-ray emission is enhanced. Based on our SRCUT model fits, X-ray emission in SW and NE filaments implies the 1 GHz radio flux of $0.7\text{--}1.5 \times 10^{-4}$ Jy, while the MOST 843 MHz image of the SNR suggests ~ 0.1 Jy for these regions (assuming that the total 1 GHz flux for the entire SNR is 5 Jy, Green 2001). Although our radio flux estimates are crude and should be considered only as an order-of-magnitude approximation based on a simple “normalization” of the total image intensity to the area corresponding to the X-ray-bright SW and NE filaments, the discrepancy is substantial by three orders of magnitudes, and should thus be real. We do not have an immediate answer as to what causes the large difference between the modeled and observed radio fluxes corresponding to the X-ray bright filaments. One speculation is that the radio spectral index might not be uniform across the SNR. While the overall radio spectrum is fitted by $\alpha = 0.3$, the faint radio filaments corresponding to the bright X-ray shell might have a steeper spectrum. For instance, if we assume a plausible range of the *observed* radio flux $\sim 0.01\text{--}0.1$ Jy for the SW region and vary the radio spectral index in our SRCUT model fit, we obtain a best-fit $\alpha \sim 0.53\text{--}0.66$ ($\chi^2_{\nu} = 1.2$). These radio spectral indices are not unusual for shell-type SNRs (Green 2001). The best-fit roll-off frequencies are high, but are poorly constrained ($\nu_{\text{rolloff}} = 13_{-9}^{+93} \times 10^{17}$ Hz when the 1 GHz radio flux of 0.1 Jy is assumed, and $\nu_{\text{rolloff}} = 8_{-6}^{+25} \times 10^{17}$ Hz for the radio flux of 0.01 Jy). Although the high roll-off frequency, $\nu_{\text{rolloff}} \sim 10^{18}$ Hz, implies somewhat higher estimates for the shock velocity and the maximum electron energy, these changes do not make a significant effect on our conclusions presented here. High resolution radio observations with a deep exposure would be essential to study the detailed relationship between the X-ray and the radio emission in this SNR.

6.3. Thermal X-Ray Emission of the Supernova Remnant

In the E region, soft thermal emission is a significant component in the observed X-ray spectrum. The best-fit electron temperature is $kT \sim 0.7\text{--}1.4$ keV, depending on models (§ 5). The best-fit ionization timescale appears to be high ($n_e t \gtrsim 10^{13}$ cm $^{-3}$ s) suggesting that the plasma could be in collisional ionization equilibrium, but the $n_e t$ parameter is not well-constrained because

of the low photon statistics. Detecting thermal emission in SNRs in which nonthermal emission dominates is critical to reveal the environmental conditions (e.g., ambient density) and the supernova energetics that should have affected the SNR evolution and the particle acceleration. In fact, G330.2+1.0 is the only example to reveal thermal X-ray emission among the four Galactic SNRs which have been known to be dominated entirely by nonthermal X-rays (see § 1). Therefore, although it is difficult to perform a thorough spectral analysis of thermal emission and to draw firm conclusions on the nature of the SNR because of the poor photon statistics for the faint thermal component, we present a brief discussion on some fundamental SNR parameters based on our spectral analysis of region E.

Based on the best-fit volume emission measure ($EM = n_e n_H V$, where n_e , n_H , and V are the postshock electron, proton densities, and the X-ray emitting volume, respectively), we estimate $n_e \sim 0.4\text{--}0.5 f^{-\frac{1}{2}} d_5^{-\frac{1}{2}} \text{ cm}^{-3}$ (where f is the X-ray emitting volume filling factor). These postshock electron densities correspond to the preshock hydrogen density $n_0 \sim 0.1 f^{-\frac{1}{2}} d_5^{-\frac{1}{2}} \text{ cm}^{-3}$. In these estimates, we assume $n_e = 1.2 n_H$ for the mean charge state with normal composition, and $n_H = 4n_0$ for a strong shock. We use the emission volume $V \sim 4 \times 10^{56} \text{ cm}^{-3}$ assuming that the path-length through region E is comparable to the physical size corresponding to the angular size ($\sim 2'$) of region E at $d = 5 \text{ kpc}$. Assuming an ion-electron temperature equilibration, the measured electron temperature implies a shock velocity of $v_s \sim 800$ ($kT = 0.7 \text{ keV}$) – 1100 ($kT = 1.4 \text{ keV}$) km s^{-1} . However, equipartition of the electron-ion temperatures may not have been reached, and thus the actual shock velocity could be higher than $v_s \sim 1000 \text{ km s}^{-1}$, probably by a factor of a few (§ 6.2). We estimate the SNR radius of $R \sim 5'$ (the half of the angular distance between the the bright SW and NE filaments), which corresponds to the physical distance of $\sim 7.3 d_5 \text{ pc}$. Then, assuming an adiabatic phase for the SNR, we apply the Sedov solution to derive the SNR age $\tau_{\text{SNR}} \sim 1100 d_5 \text{ yr}$ (e.g., for $v_s \sim 2500 \text{ km s}^{-1}$, § 6.2). For a free-expansion phase, the SNR age is also derived to be $\tau_{\text{SNR}} \sim 1100 \text{ yr}$ (e.g., for $v_s \sim 6500 \text{ km s}^{-1}$, § 6.2). Using a Sedov solution, the explosion energy is estimated to be $E_0 \sim 2\text{--}9 \times 10^{50} d_5^{\frac{5}{2}} \text{ ergs}$ for $\tau_{\text{SNR}} \sim 1000\text{--}2000 \text{ yr}$.

7. Summary and Conclusions

Based on the *ASCA* data, the overall X-ray emission from SNR G330.2+1.0 was suggested to be continuum-dominated with no evidence for line features (Torii et al. 2006). The high resolution *Chandra* images subsequently revealed that X-ray emission from this SNR originates primarily from the thin shell with enhanced filaments in the SW and NE parts of the shell (Park et al. 2006). Park et al. (2006) have also discovered the CCO J1601 at the center of the SNR. We performed follow-up observations of G330.2+1.0 with *XMM-Newton* to investigate the nature of the CCO and the SNR. Although our spectral and temporal analyses of J1601 and G330.2+1.0 are limited by poor photon statistics of the *XMM-Newton* data caused by significant contamination from flaring particle background, we find several important characteristics of these objects utilizing the *XMM-Newton*

and *Chandra* data.

The X-ray spectrum of J1601 can be described by two-component neutron star atmosphere models. X-ray emission primarily originates from a small hot region ($R \sim 0.4\text{--}2$ km, $T \sim 2.5\text{--}5.5$ MK). The rest of the neutron star's surface is cooler ($R \sim 10$ km, $T < 1.5$ MK), suggesting an $\gtrsim 10^{3-4}$ yr old neutron star based on the standard cooling models. The neutron star atmosphere models do not provide useful constraints on the magnetic field of J1601 with the current data. The previously suggested pulsations ($P \sim 7.48$ s) are not confirmed by the *XMM-Newton* data. These characteristics are similar to those found for CCOs in other Galactic SNRs such as Cas A and Vela Jr. The spectrally hard, faint nebulosity at $\sim 2'$ SW from the CCO could be the associated PWN, but its true nature is uncertain with the current data because of the poor photon statistics. Follow-up deep X-ray observations are required to reveal the detailed nature of J1601.

Assuming that X-ray emission in the shell of G330.2+1.0 is synchrotron radiation from the shock accelerated electrons, the roll-off frequency of $\nu_{\text{rolloff}} \sim 1.6\text{--}3.3 \times 10^{17}$ Hz is estimated. It is difficult to measure the shock velocity with the currently available data. Based on several independent approaches, we make a rough estimate of the shock velocity $v_s \sim 4000$ km s $^{-1}$ (with a factor of ~ 2 uncertainty). Based on this shock velocity and the measured roll-off frequency, we find that the particle (electron) acceleration in G330.2+1.0 is likely limited by synchrotron losses rather than the SNR age. Using the *Chandra* images, we measure the widths of the bright nonthermal X-ray filaments ($D \sim 0.3\text{--}0.4$ pc). Using these widths and the shock velocity, we estimate the synchrotron loss time of $\tau_{\text{loss}} \sim 350\text{--}600$ yr and the magnetic field of $B \sim 10\text{--}50$ μ G. The maximum electron energy is derived to be $E_{\text{max}} \sim 22\text{--}38$ TeV. These electron energies suggest that G330.2+1.0 is a candidate γ -ray source (up to \sim TeV) by the IC scattering of the CMB photons. The non-detection of G330.2+1.0 in the current H.E.S.S. survey with a short exposure is perhaps expected, because G330.2+1.0 is more distant and likely a fainter γ -ray source than the bright TeV SNRs like G347.3–0.5 and Vela Jr.

G330.2+1.0 is particularly intriguing because this is the only SNR in which we detect a thermal component among the four Galactic SNRs known to be dominated by nonthermal X-ray emission. Although the uncertainties are large due to the poor photon statistics, the estimated density ($n_0 \sim 0.1$ cm $^{-3}$) is low, suggesting that γ -ray emission, if it exists, would be dominated by the IC process. The detection of γ -ray emission as well as thermal X-ray emission with high photon statistics from G330.2+1.0 will be essential to test and constrain models for γ -ray production from shock-accelerated particles. Follow-up deep observations with X-ray detectors on board *XMM-Newton* and *Suzaku* are necessary for a thorough study of thermal X-ray emission. Deep γ -ray observations using *Fermi* and the ground-based TeV telescopes will be critical to reveal the nature of nonthermal radiation produced by shock accelerated particles. High resolution radio and X-ray observations of G330.2+1.0 with a deep exposure are essential to reveal the origin of the apparent inconsistency between the radio and nonthermal X-ray emission, such as the radio spectral index variation across the SNR.

The authors thank V. E. Zavlin for the helpful discussion on the hydrogen neutron star atmosphere models. This work was supported in parts by NASA grant NNX08AW88G and SAO grant SV4-74018. POS acknowledges partial support from NASA contract NAS8-03060. KM was partially supported by the Grant in-Aid for Young Scientists (B) of the MEXT (No. 18740108). This work makes use of the *Supernova Remnant Catalog* by the MOST which is operated by the University of Sydney with support from the Australian Research Council and the Science Foundation for Physics within the University of Sydney.

REFERENCES

- Aharonian, F. et al. 2004, *Nature*, 432, 75
- Aharonian, F. et al. 2005, *A&A*, 437, L7
- Aharonian, F. et al. 2006a, *ApJ*, 636, 777
- Aharonian, F. et al. 2006b, *A&A*, 449, 223
- Anders, E. & Grevesse, N. 1989, *Geochimica et Cosmochimica Acta* 53, 197
- Ballet, J. 2006, *AdSpR*, 37, 1902
- Bamba, A., Yamazaki, R., Ueno, M., & Koyama, K. 2003, *ApJ*, 589, 827
- Bamba, A., Yamazaki, R., Yoshida, T., Terasawa, T., & Koyama, K. 2005, *ApJ*, 621, 793
- Bignami, G. F., Caraveo, P. A., De Luca, A., & Mereghetti, S. 2003, *Nature*, 423, 725
- Borkowski, K. J., Lyerly, W. J. & Reynolds, S. P. 2001, *ApJ*, 548, 820
- Buccheri, R., et al. 1983, *A&A* 128, 245
- Ellison, D. C., Berezhko, E. G., & Baring, M. G. 2000, *ApJ*, 540, 292
- Ellison, D. C., Decourchelle, A., & Ballet, J. 2004, *A&A*, 413, 189
- Ellison, D. C., Patnaude, D. J., Slane, P. O., Blasi, P., & Gabici, S. 2007, *ApJ*, 661, 879
- Ghavamian, P., Laming, J. M., & Rakowski, C. E. 2007, *ApJ*, 654, L69
- Green, D. A. 2001, *A Catalog of Galactic Supernova Remnants* (2001 December version), Mullard Radio Astronomy Observatory, Cavendish Laboratory, Cambridge, UK (<http://www.mrao.cam.ac.uk/surveyssnrs>)
- Katz, B. & Waxmann, E. 2008, *J. Cosmology & Astroparticle Phys.*, 1, 18

- Koyama, K., Petre, R., Gotthelf, E. V., Hwang, U., Matsuura, M., Ozaki, M., & Holt, S. S. 1995, *Nature*, 378, 255
- Lazendic, J. S., Slane, P. O., Gaensler, B. M., Reynolds, S. P., Plucinsky, P. P., & Hughes, J. P. 2004, *ApJ*, 602, 271
- Matsumoto, H. et al. 2007, *PASJ*, 59, S199
- McClure-Griffiths, N. M., Green, A. J., Dickey, J. M., Gaensler, B. M., Haynes, R. F., & Wieringa, M. H. 2001, *ApJ*, 551, 394
- Parizot, E., Marcowith, A., Ballet, J., & Gallant, Y. A. 2006, *A&A*, 453, 387
- Park, S., Mori, K., Kargaltsev, O., Slane, P. O., Hughes, J. P., Burrows, D. N., Garmire, G. P., & Pavlov, G. G. 2006, *ApJ*, 653, L37
- Pavlov, G. G., Shibanov, Yu.A., Zavlin, V. E., & Meyer, R. D. 1995, in *The Lives of the Neutron Stars*, eds. M. A. Alpar, U. Kiziloglu, & J. van Paradijs (NATO ASI Ser. C, 450; Dordrecht: Kluwer), p. 71
- Pavlov, G. G., Zavlin, V. E., Aschenbach, B., Trümper, J., & Sanwal, D. 2000, *ApJ*, 531, L53
- Pavlov, G. G. & Zavlin, V. E. 2000, in *High Energetic Physical Processes and Mechanisms for Emission from Astrophysical Plasmas*, IAU Symposium, Vol. 195, 103, eds. P. C. H. Martens, S. Tsuruta, & M. A. Weber
- Pavlov, G. G., Sanwal, D., Kiziltan, B., & Garmire, G. P. 2001, *ApJ*, 559, L131
- Pavlov, G. G., Sanwal, D., Garmire, G. P., & Zavlin, V. E. 2002, in *Neutron Stars in Supernova Remnants*, ASP Conf. Ser., Vol. 271, eds., P. O. Slane & B. M. Gaensler (San Francisco: ASP), p. 247
- Pavlov, G. G., Sanwal, D., & Teter, M. 2004, in *Young Neutron Stars and Their Environments*, IAU Symposium 218, eds., F. Camilo & B. Gaensler (San Francisco: ASP), 239
- Reynolds, S. P. 1998, *ApJ*, 493, 375
- Reynolds, S. P. & Keohane, J. W. 1999, *ApJ*, 525, 368
- Reynolds, S. P., Borkowski, K. J., Green, D. A., Hwang, U., Harrus, I., & Petre, R. 2008, *ApJ*, 680, L41
- Slane, P. O., Gaensler, B. M., Dame, T. M., Hughes, J. P., Plucinsky, P. P., & Green, A. 1999, *ApJ*, 525, 357
- Slane, P. O., Hughes, J. P., Edgar, R. J., Plucinsky, P. P., Miyata, E., Tsunemi, H., & Aschenbach, B. 2001, *ApJ*, 548, 814

- Tatischeff, V. 2008, in *Supernovae: Lights in the Darkness (XXIII Trobades Cientifiques de la Mediterrania)*, October 3-5, 2007, Mao, Menorca Spain (PoS), arXiv0804.1004
- Torii, K., Uchida, H., Hasuike, K., Tsunemi, H., Yamauchi, Y., & Shibata, S. 2006, *PASJ*, 58, L11
- Tsuruta, S. 1998, *Phys. Rep.*, 292, 1
- Whiteoak, J. B. Z. & Green, A. J. 1996, *A&AS*, 118, 329
- Yakovlev, D. G. & Pethick, C. J. 2004, *ARA&A*, 42, 169
- Zavlin, V. E., Pavlov, G. G., & Shibanov, Yu.A. 1996, *A&A*, 315, 141
- Zavlin, V. E., Pavlov, G. G., & Trümper, J. 1998, *A&A*, 331, 821
- Zavlin, V. E., Pavlov, G. G., Sanwal, D., & Trümper, J. 2000, *ApJ*, 540, L25

Table 1. Best-Fit Parameters of J1601 from two-component neutron star atmosphere models.

B (10^{12} G)	N_H (10^{22} cm^{-2})	T_s^∞ ^a (10^6 K)	T_h^∞ ^a (10^6 K)	R_h ^b (d_5 km)	$f_{1-10 \text{ keV}}$ ^c (10^{-13} ergs cm^{-2} s^{-1})	$L_{1-10 \text{ keV}}$ (10^{33} d_5^2 ergs s^{-1})	χ^2/ν
0	$3.15^{+0.63}_{-0.35}$	< 1.4	$2.5^{+0.3}_{-0.2}$	$2.1^{+2.3}_{-0.6}$	1.23 ± 0.06	1.5	80.5/78
1	$3.40^{+0.52}_{-0.20}$	< 1.5	$5.5^{+0.4}_{-0.3}$	$0.4^{+0.1}_{-0.1}$	1.21 ± 0.06	1.9	79.9/78
10	$3.29^{+0.53}_{-0.88}$	< 1.5	$3.7^{+0.6}_{-0.4}$	$0.9^{+0.6}_{-0.3}$	1.21 ± 0.06	1.8	79.7/78

Note. — Errors are at 90% confidence. M_{ns} and R_{ns} are fixed at $1.4 M_\odot$ and 10 km, respectively.

^a T_s^∞ and T_h^∞ are effective temperatures of the cool neutron star surface and the hot small region, respectively, as measured by a distant observer where $T^\infty = g_r T$ and $g_r = (1 - 2GM_{\text{ns}}/R_{\text{ns}}c^2)^{\frac{1}{2}}$.

^bThe radius of the hot region scaled by $d = 5$ kpc.

^cThe observed flux in the 1–10 keV band. Assuming a Poisson distribution of the observed photon statistics, 2σ statistical errors are quoted.

Table 2. Best-Fit Power Law Model Parameters for SNR G330.2+1.0.

Region	N_H (10^{22} cm^{-2})	Γ	kT (keV)	$n_e t$ (10^{11} cm^{-3} s)	EM (10^{56} cm^{-3})	χ^2/ν
SW	$2.60^{+0.40}_{-0.34}$	$2.13^{+0.24}_{-0.22}$	-	-	-	163.9/137
NE	$3.04^{+0.65}_{-0.81}$	$2.52^{+0.40}_{-0.54}$	-	-	-	51.9/51
E	$2.45^{+0.72}_{-0.57}$	2.3	$0.70^{+1.34}_{-0.32}$	> 5	$1.4^{+6.8}_{-1.0}$	35.3/30

Note. — Errors are at 90% confidence. For region E, parameters from the best-fit two component model (plane-shock + power law, where $\Gamma = 2.3$ is fixed) are presented.

Table 3. Best-Fit SRCUT Model Parameters for SNR G330.2+1.0.

Region	N_H (10^{22} cm^{-2})	ν_{rolloff} (10^{17} Hz)	1 GHz Flux (mJy)	χ^2/ν
SW	$2.41^{+0.17}_{-0.15}$	$3.3^{+4.1}_{-1.7}$	0.15 ± 0.01	163.7/137
NE	$2.59^{+0.32}_{-0.28}$	$1.6^{+4.0}_{-1.1}$	0.07 ± 0.01	51.9/51

Note. — Errors are at 90% confidence. The radio spectral index is fixed at $\alpha = 0.3$ (where $S_\nu \propto \nu^{-\alpha}$).

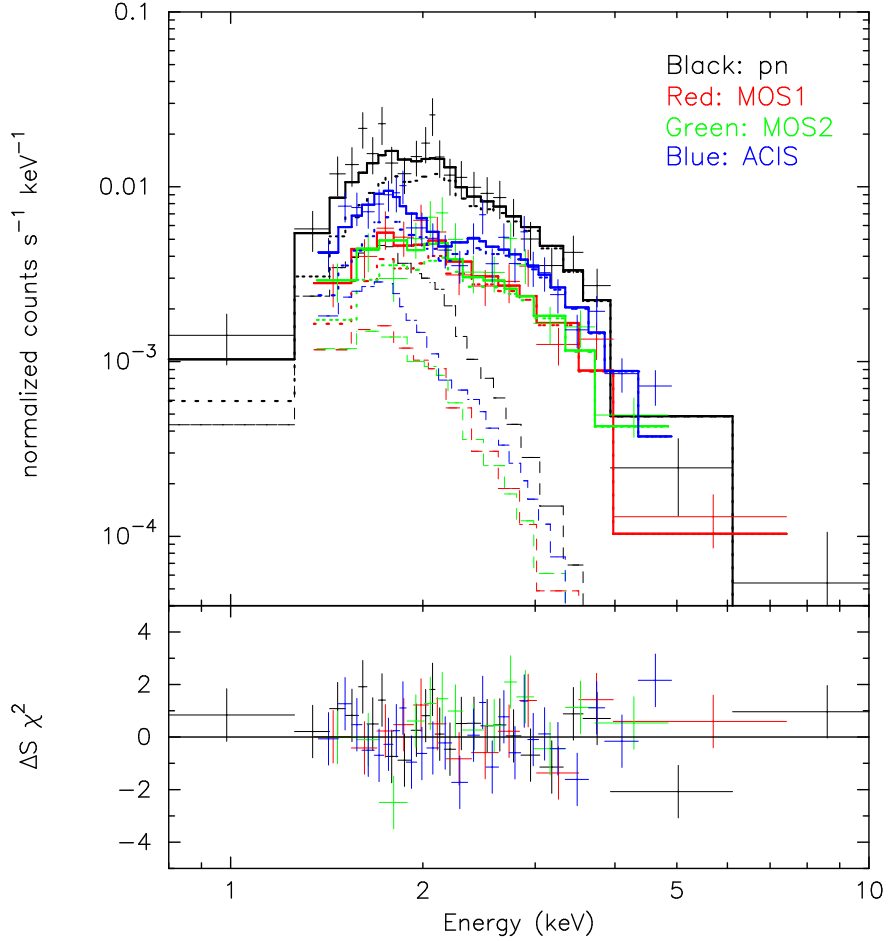


Fig. 1.— The X-ray spectrum of J1601 as observed by *XMM-Newton* and *Chandra*. The best-fit two component NSA model with $B = 10^{13}$ G is overlaid. The solid lines are the best-fit model. The dotted- and dashed-lines are the small hot region and the large cool surface components, respectively. The lower panel is the residuals from the best-fit model.

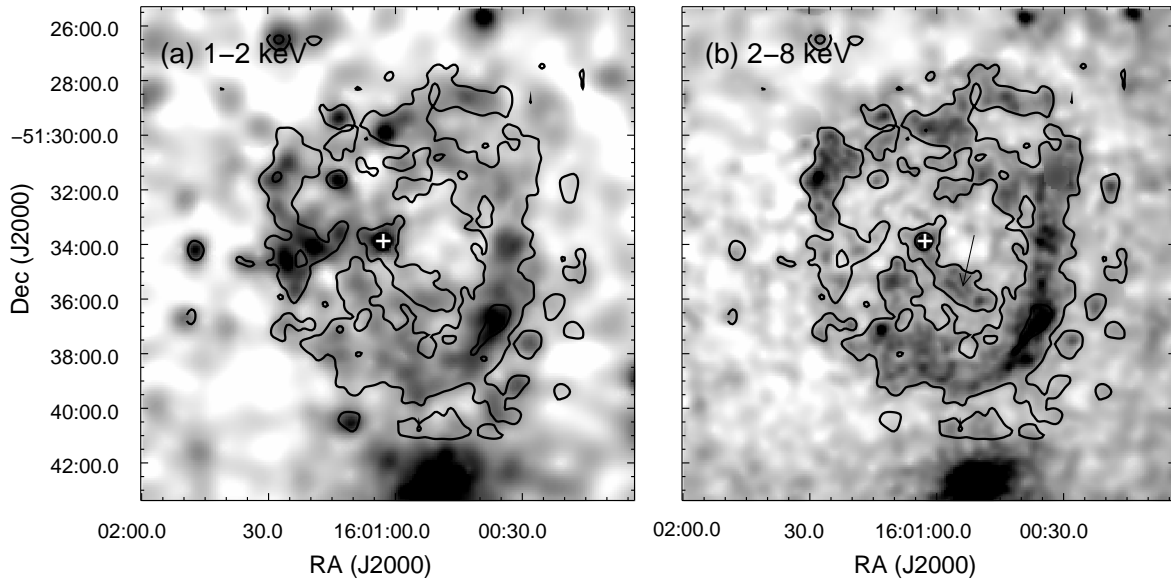


Fig. 2.— *XMM-Newton* images (MOS1+MOS2) of G330.2+1.0: (a) the soft band (1–2 keV), and (b) the hard band (2–8 keV). In (a), the 1.4–1.6 and 1.7–1.8 keV bands are excluded to remove the bright instrumental lines at $E \sim 1.5$ (Al K) and 1.74 (Si K) keV. Images are exposure-corrected, and darker grey-scales correspond to higher intensities. For the purposes of display, the images have been binned into $\sim 5''$ pixels, and then adaptively smoothed to achieve a minimum S/N = 7. J1601 is marked with a cross at the center of the SNR. Image contours of the broadband (1–8 keV) image are overlaid in each panel. In (b), the hard feature seen in Fig. 3 is marked with an arrow.

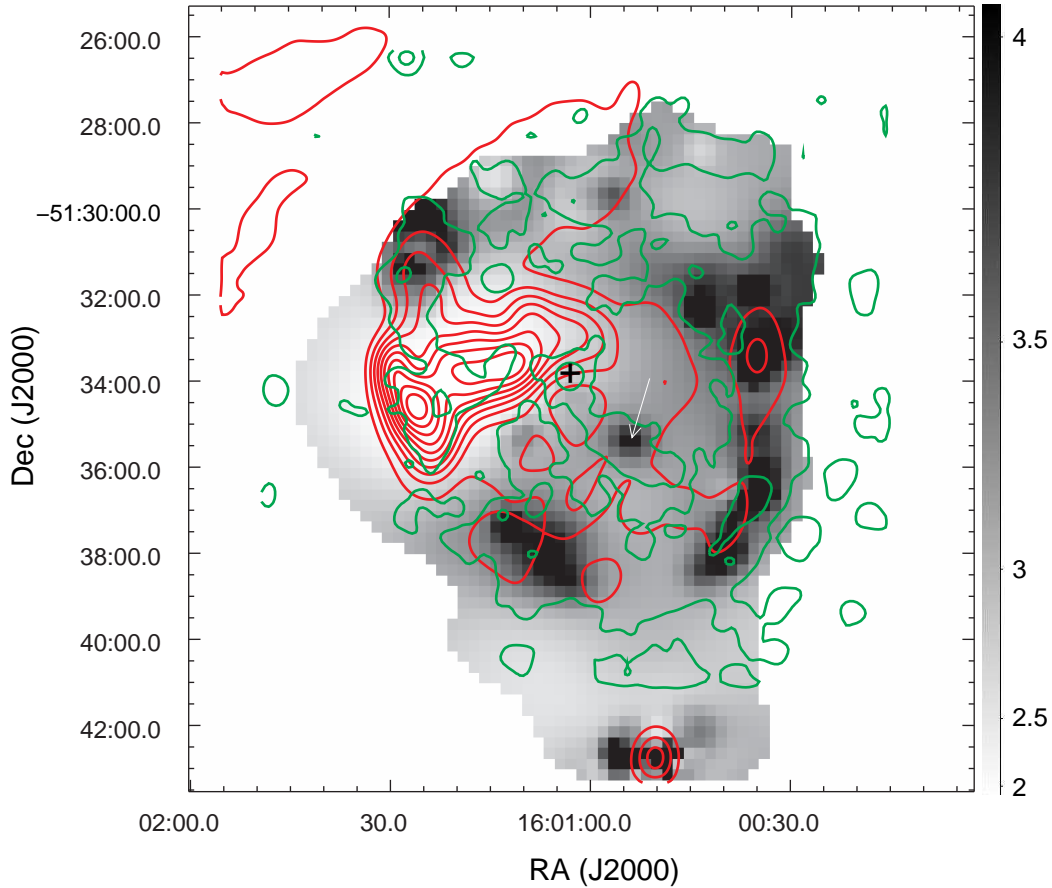


Fig. 3.— The 2–8 keV to 1–2 keV hardness ratio map of G330.2+1.0 as obtained by the *XMM-Newton* EPIC MOS1+MOS2. In the soft band (1–2 keV) map, the 1.4–1.6 and 1.7–1.8 keV bands are excluded to remove the bright instrumental lines at $E \sim 1.5$ and 1.74 keV. For the purposes of display, each image has been binned into $15'' \times 15''$ pixels, and is adaptively smoothed to achieve a minimum $S/N = 4$. Green image contours are the 1–8 keV image of the SNR as shown in Fig. 2. Red contours are the 843 MHz radio image taken from the MOST Supernova Remnant Catalog (Whiteoak & Green 1996). The angular resolution of the radio image is $43''$. The position of the CCO J1601 is marked with a cross. The hard feature in the SW of the CCO is marked with a white arrow.

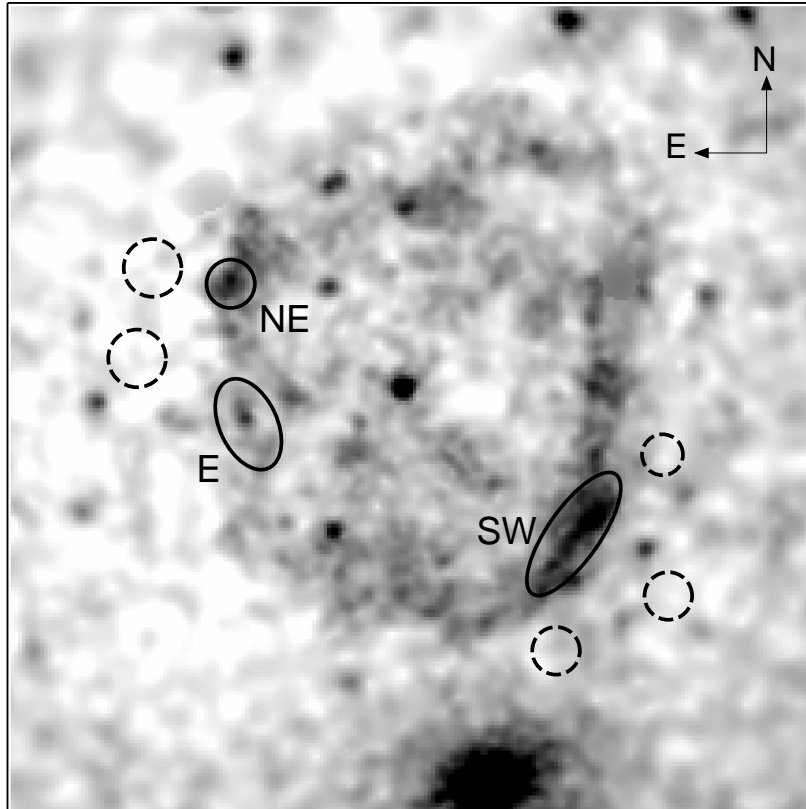


Fig. 4.— The broadband (1–8 keV) grey-scale image of G330.2+1.0 obtained by *XMM-Newton* EPIC MOS1+MOS2. The image has been processed in the same way as those in Fig. 2. SW, NE, and E regions of the SNR shell are marked with solid lines. Background regions are marked with dashed circles.

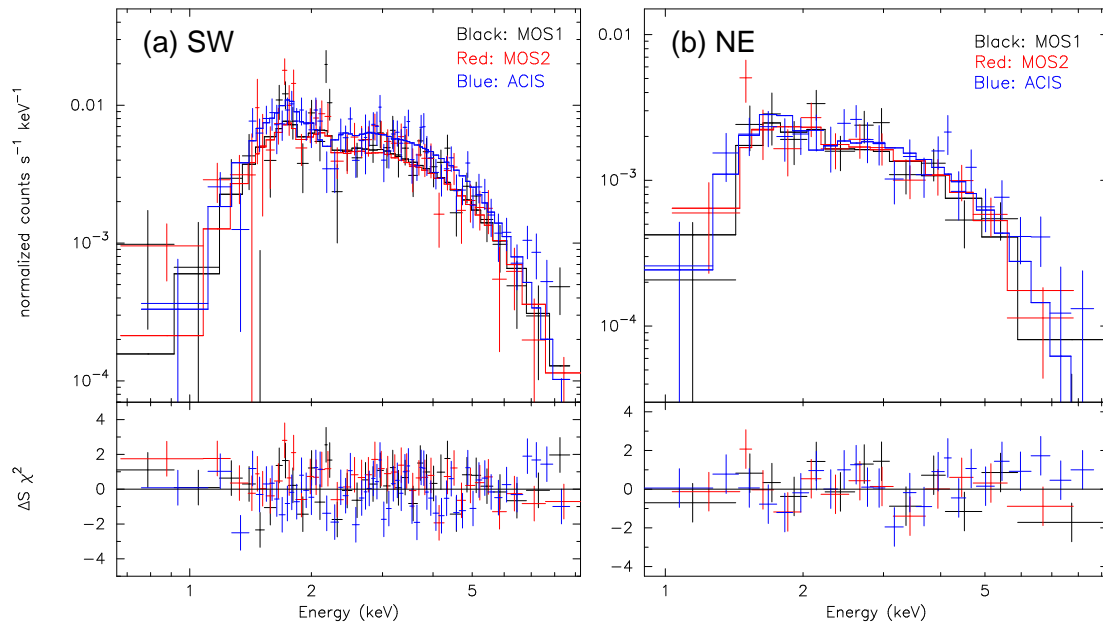


Fig. 5.— The X-ray spectrum from the shell of G330.2+1.0. (a) The SW, and (b) the NE shell. The best-fit power law model for each regional spectrum is overlaid. The lower panels are the residuals from the best-fit model.

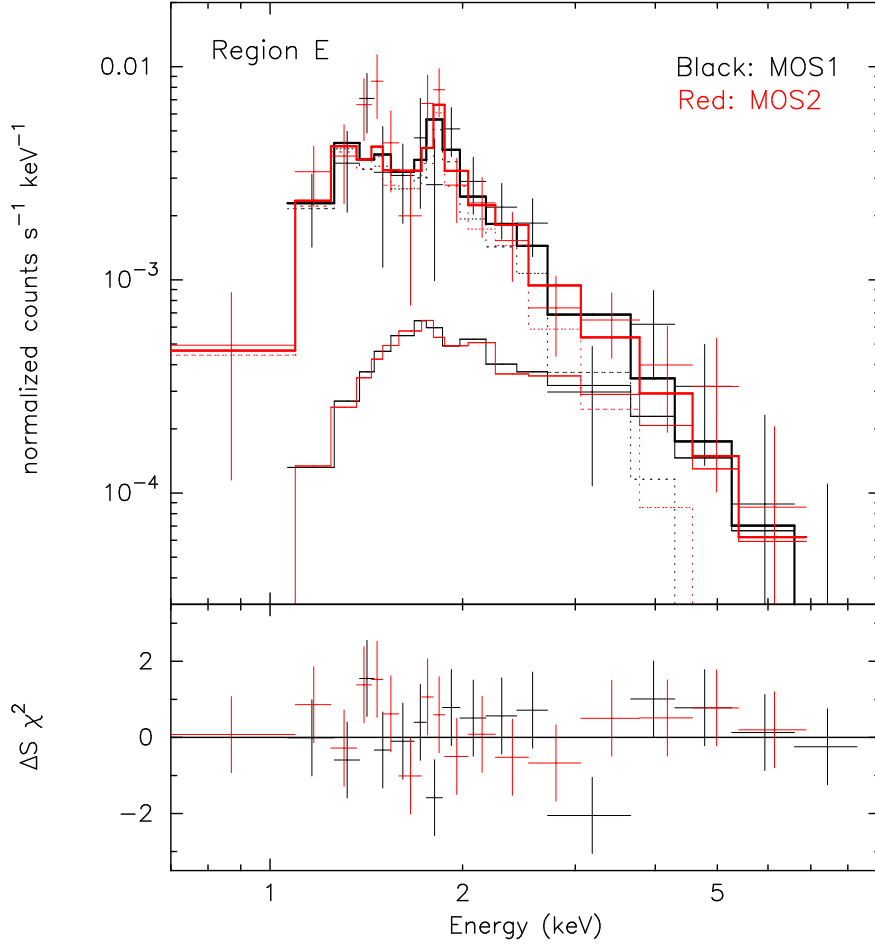


Fig. 6.— The X-ray spectrum from region E of G330.2+1.0. The best-fit two component model (thick solid lines) is overlaid. The dotted and the thin solid lines are the plane-shock ($kT = 0.7$ keV) and the power law ($\Gamma = 2.3$) components, respectively. The lower panel is the residuals from the best-fit model.

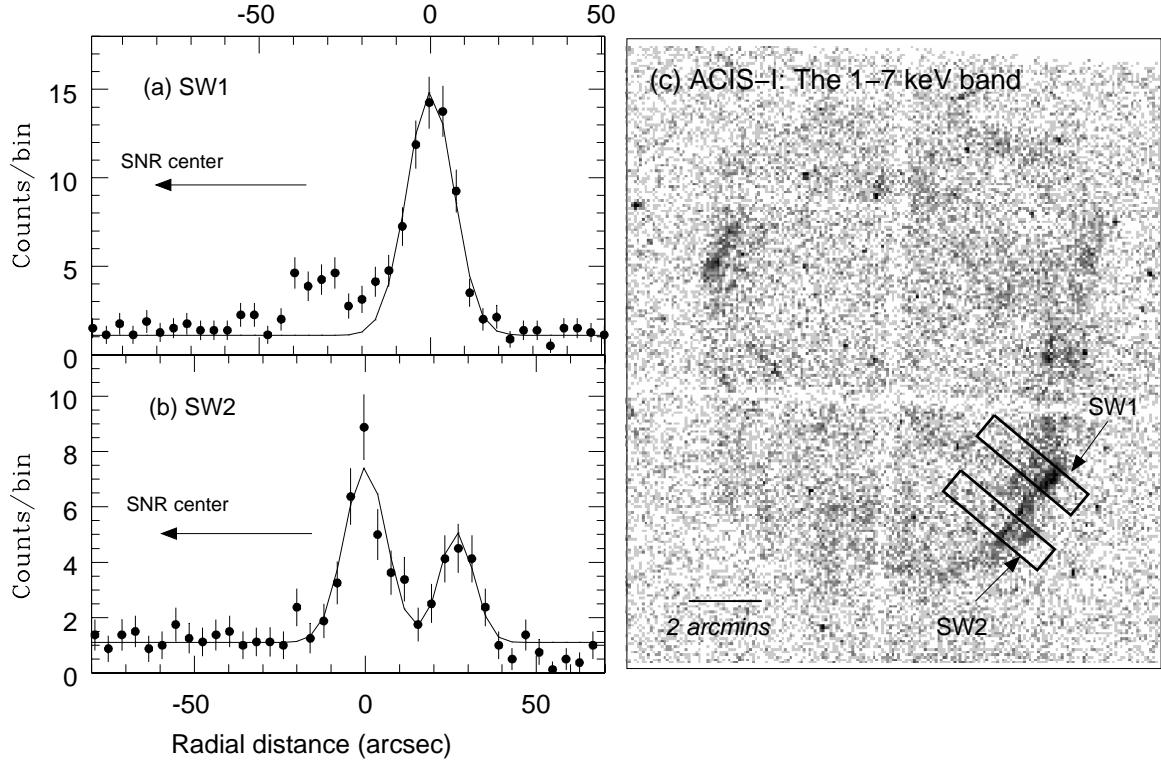


Fig. 7.— Radial intensity profiles of the SW shell of G330.2+1.0 obtained by the *Chandra* data. (a) The bright northern parts (SW1) and (b) the faint southern parts (SW2) of the SW shell. (c) The 1–7 keV band *Chandra* ACIS-I image of G330.2+1.0. SW1 and SW2 regions ($180'' \times 40''$ for each region) are marked. The image has been binned into $4''$ size pixels for the purposes of display. In (a) and (b), each regional image has been binned into 8×8 pixels ($\sim 4''$ size), and then is averaged over $40''$ column along the shell to produce a projected 1-D radial intensity profile. The best-fit Gaussian model (with a constant underlying background) is overlaid. In (a), the small intensity bump just inside of the shell ($\sim 25''$ – $45''$ toward the SNR center) is excluded in the fit.